






# A novel heat dissipation structure based on flat heat pipe for battery thermal management system

Yueqi Wang<sup>1</sup> | Dan Dan<sup>1,2</sup> | Yangjun Zhang<sup>1</sup>  | Yuping Qian<sup>1</sup> |  
Satyam Panchal<sup>3</sup>  | Michael Fowler<sup>4</sup>  | Weifeng Li<sup>1</sup> | Manh-Kien Tran<sup>4</sup>  |  
Yi Xie<sup>5</sup> 

<sup>1</sup>State Key Laboratory of Automotive Safety and Energy, School of Vehicle and Mobility, Tsinghua University, Beijing, China

<sup>2</sup>School of Mechanical Engineering, Beijing Institute of Technology, Beijing, China

<sup>3</sup>Department of Mechanical and Mechatronics Engineering, University of Waterloo, Waterloo, Ontario, Canada

<sup>4</sup>Department of Chemical Engineering, University of Waterloo, Waterloo, Ontario, Canada

<sup>5</sup>College of Mechanical and Vehicle Engineering, Chongqing University, Chongqing, China

## Correspondence

Yangjun Zhang, State Key Laboratory of Automotive Safety and Energy, School of Vehicle and Mobility, Tsinghua University, Beijing 100084, China.  
Email: [yjzhang@tsinghua.edu.cn](mailto:yjzhang@tsinghua.edu.cn)

Yi Xie, College of Mechanical and Vehicle Engineering, Chongqing University, Chongqing, 400044, China.  
Email: [claudexie@cqu.edu.cn](mailto:claudexie@cqu.edu.cn)

## Funding information

State Key Laboratory of Automotive Safety and Energy, Grant/Award Number: ZZ2019-051; National Natural Science Foundation of China, Grant/Award Numbers: U20A20310, U1864212

## Summary

Flying car is an effective transport to solve current traffic congestion. The power batteries in flying cars discharge at a high current rate in the takeoff and landing phase, evoking a severe thermal issue. Flat heat pipe (FHP) is a relatively new type of battery thermal management technology, which can effectively maintain the temperature uniformity of the battery pack. We have constructed a resistance-based thermal model of the batteries considering the impact of the state of charge (SOC), battery temperature, and current on the battery heat generation. The FHP model is developed based on segmental heat conduction model, and integrated into the battery model to form the battery-FHP-coupled model for a battery module. Experiments are carried out to verify its accuracy. Then, the battery thermal performance is analyzed under the different discharging conditions including constant discharge rates and dynamic discharge rates for flying cars. Under the condition of the flying cars, the battery maximum temperature appears at the end of takeoff stage, while the maximum temperature difference appears during the forward flight segment. Moreover, different FHP heat dissipation structures are studied to further improve the battery thermal performance. The configuration with the best performance is adopted for the battery pack, and it can meet the heat dissipation requirements of the pack at a discharge rate of 3C or that of flying cars. Finally, the influence of inlet cooling air velocity and temperature on battery thermal performance is investigated. According to the research results, air velocity has little effect on the battery maximum temperature at the discharge rate of flying cars, but it can obviously affect the temperature decrease rate. Besides, the battery maximum temperature and its temperature difference develop linearly with the air temperature.

**Abbreviations:** BTMS, battery thermal management system; CFD, computational fluid dynamics; FHP, flat heat pipe; GUI, graphical user interface; NCM, nickel cobalt manganese; OCV, open circuit voltage; PCM, phase change material; SOC, state of charge.

Yueqi Wang and Dan Dan contributed equally to this work.

**KEYWORDS**

battery thermal management system, flat heat pipe, flying car, power battery, thermal performance

## 1 | INTRODUCTION

Advances in the automobile industry have exacerbated traffic conditions, raising people's economic, and life expenses. The electric vertical takeoff and landing aircraft (eVTOL or flying car) which can fly in the air intends to alleviate traffic congestion and has been a hot discussion topic among researchers and the public.<sup>1</sup> Power batteries significantly affect the fully electronic system of flying cars. The critical aspect of designing flying cars is determining whether the power batteries meet the operational requirements.<sup>2</sup> The related research works<sup>3,4</sup> have demonstrated that the power batteries should have high power density and high specific energy. The battery pack should operate at a high discharge rate (above 4C) during takeoff and landing segments, and the peak discharge rate should be around 5C. Lithium-ion battery is regarded as one of the promising power batteries for flying cars because of the high energy/power density, low self-discharge rate and extended lifespan.<sup>5,6</sup> However, the lithium-ion battery cells are very sensitive to the temperature.<sup>7</sup> The high discharge rate causes high-temperature rise and high-temperature difference in the batteries, affecting their lifespan and the overall performance.<sup>8,9</sup> Therefore, a proper battery thermal management system (BTMS) is crucial for maintaining battery packs within the appropriate temperature range.<sup>10</sup> The optimal operating temperature range of lithium-ion batteries is 25–40°C, and the temperature difference is no more than 5°C.<sup>11,12</sup> Some researchers have regarded 45°C as an upper limit of the maximum temperature for BTMS in some moderate operating conditions.<sup>13</sup>

There is a small amount of research on flying cars' battery thermal management and operating conditions. However, various cooling techniques for BTMS, such as air cooling, liquid cooling, phase change principle-based cooling and the combination of the abovementioned approaches, have been developed for electric vehicles.<sup>14</sup> Different from battery thermal management for electric vehicles, batteries in flying cars have higher transient discharge rate and more special boundary conditions (such as at higher or lower ambient temperatures). Moreover, flying cars have a higher requirement for the lightweight of the BTMS. However, the current battery thermal management methods for electric vehicles can provide corresponding guidance for the BTMS in flying cars in certain

degrees. Air cooling is widely used in the BTMS of electric vehicles because of its simple and lightweight structure and low costs.<sup>15</sup> However, the air-cooling system exhibits a poor heat dissipation effect and a non-uniform temperature distribution,<sup>16</sup> especially under a high charge/discharge rate in the flying cars operating conditions. Liquid cooling is more effective for heat dissipation than air cooling because of its higher heat transfer coefficient.<sup>17</sup> It can easily maintain the maximum temperature of the battery below 45°C at a discharge rate of less than 2C.<sup>18</sup> Nevertheless, the liquid cooling components increase the system weight and leakage risk<sup>19</sup> while lowering the power to weight ratio of the flying car electric propulsion system. Phase change material (PCM)-based BTMS has garnered increased traction nowadays, further leading to the development of a more uniform temperature distribution.<sup>20</sup> However, the lower thermal conductivity of PCM delays heat dissipation from the battery system,<sup>21</sup> especially at high discharge rates.

A heat pipe operating on gas-liquid phase change principles is a type of high-efficiency heat transfer element. It has high thermal conductivity and is lightweight, allowing relatively better heat dissipation when combined with the air cooling or liquid cooling technology.<sup>22,23</sup> Heat pipes for BTMS have received substantially more attention recently. Researchers integrated heat pipes with other cooling methods to improve the thermal performance of batteries.<sup>24,25</sup> For example, Wu et al<sup>26</sup> compared natural convection, forced convection, and heat pipe-based air-cooling methods on the battery thermal performance. They discovered that the combination of heat pipe and air cooling appears to be effective for reducing battery temperature rise and controlling temperature uniformity. Behi et al<sup>27</sup> presented a heat pipe embedded with copper sheets in BTMS and combined it with air cooling at the condensation section. Their results indicated the lowering of battery maximum temperature up to 42.7% and improvement of the temperature uniformity by 73.4% compared to natural air cooling. Yuan et al<sup>28</sup> proposed a battery liquid cooling structure comprising a heat pipe and cooling plate. The new structure can control battery maximum temperature at 34.1°C and reduce temperature difference at 1°C under the discharge rate of 2C and an ambient temperature of 30°C. The feasibility of the heat pipes in BTMS has been validated.

The flat heat pipe (FHP) can significantly increase the contact area with batteries compared to conventional one-dimensional heat pipes, efficiently flattening the battery temperature distribution and reducing thermal resistance.<sup>29</sup> Moreover, FHP can provide flexibility with the BTMS's compact structure suited for a flying car electric propulsion system. Zhao et al<sup>30</sup> designed an ultra-thin FHP and studied the thermal performance of four pouch batteries at high discharge rates. They presented wet cooling-integrated FHP-BTMS and experimentally compared it with other types of cooling methods. Gou et al<sup>31</sup> explored a novel 3D FHP (vapor chamber) in a small battery module to investigate the effects of the filling ratio and system inclinations on the battery thermal behavior. Jouhara et al<sup>32</sup> developed a test rig and mounted the battery pack on the top of the FHP cooled by water flow. The maximum battery temperature could be limited to under 35°C, and the temperature difference was controlled within 3°C at a discharge rate of 4C. The above-mentioned experimental research works reveal that the FHP-based BTMS combined with air or liquid cooling significantly improves the battery thermal characteristics. Some researchers also conducted a relative simulation analysis to determine the heat dissipation effects of FHP on BTMS. Behi et al<sup>33</sup> established a sandwiched configuration of the FHP cooling system with a forced convection system. They created a computational fluid dynamics (CFD) model to simulate the battery thermal performance under different transient boundary conditions. Zhang et al<sup>34</sup> developed a numerical model of FHP integrated with cooling fins on BTMS to effectively improve the battery thermal performance with minimum energy costs. Yao et al<sup>35</sup> proposed a novel FHP-based air conditioning system for a battery module and numerically investigated the battery temperature distribution. The results indicated that the battery temperature difference could be maintained within 3°C under the 40 W heat generation rate of each cell. Xu et al<sup>36</sup> verified thermal management effect of FHP combined with liquid cooling on a single battery pack. The highest temperature of the system could be controlled within 48°C at 2C discharge rate.

Both the experimental and simulation results in the above-mentioned studies demonstrated the heat dissipation capability of FHP in the BTMS system under certain extreme battery working conditions. Researchers mainly focused on the configuration of FHP-based BTMS and investigated the effects of system parameters on the battery thermal performance. Nevertheless, considering the different operating conditions between electric vehicles and flying cars, there are still some shortcomings in BTMS for flying car utilization. First, the discharge rate is relatively higher for the batteries in flying cars. Some

of the abovementioned research works<sup>35,36</sup> analyzed the battery thermal behavior under a low discharge rate with constant current during the discharging process. The battery discharge rate changes dynamically in flying cars and keeps above 4C at takeoff and landing segments. Researchers have not explored the battery thermal performance in FHP-based BTMS under flying cars transient operating conditions. Second, most of the research only investigated the heat dissipation effect of FHP on single battery cells<sup>30,33</sup> or a small battery module.<sup>31,32,34,35</sup> The heat transfer capacity of FHP on a battery pack was seldom considered. Third, liquid cooling is not suitable for heat dissipation due to the lightweight design requirements of flying cars. Therefore, FHP combined with air cooling is required in this situation. The configuration of FHP integrated with cooling fins in BTMS may affect the battery temperature distribution, which is not further compared and discussed in the research works. Therefore, it is meaningful to investigate the effects of FHP configurations and its structural parameters on thermal performance of the battery pack under flying cars working conditions, which could pave the way for the usage of FHP in BTMS for flying car utilization.

This research paper uses an FHP combined with an air-cooling method for the heat dissipation of prismatic batteries. Three main contributions are made compared with the existing studies. First, an FHP-based BTMS for a battery module is proposed and the model of the system is established and verified experimentally. The battery thermal performance is analyzed under different discharge rates, including the constant discharge rate and flying car discharging conditions. Second, we present four FHP configurations of the BTMS on improving battery thermal performance and compares them subsequently. An optimal layout of FHP is chosen and used on the battery pack. Its heat dissipation effectiveness is verified. Third, the influence of discharge rate, coolant air velocity, and coolant air temperature on the battery thermal characteristics are examined.

## 2 | NUMERICAL MODELS

### 2.1 | Geometric model description

First, the cooling effect of FHP-based BTMS on a battery module was analyzed. Figure 1 depicts the schematic representation of this system. Table 1 presents the parameters of a prismatic battery cell. The battery module comprises 12 battery cells with 3 parallel and 4 series arrangements. The capacity of lithium batteries used in actual flying cars are depended on many factors, such as

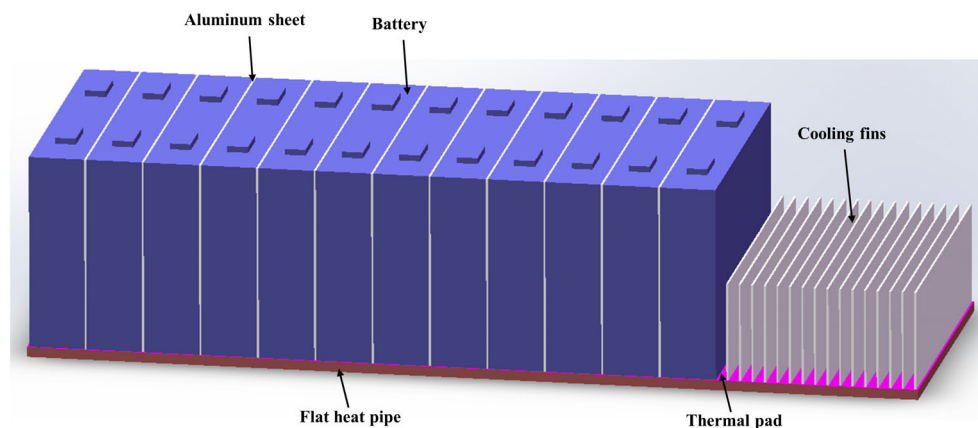


FIGURE 1 Schematic representation of FHP-based BTMS

TABLE 1 Parameters of lithium-ion battery cells

Parameters	Value (Property)
Dimensions	148.3 mm * 26.7 mm * 98 mm
Anode material	NCM
Electrolyte material	LiPF <sub>6</sub>
Cathode material	Graphite
Nominal capacity	50 Ah
Nominal voltage	3.65 V
Operating voltage	2.75 V-4.25 V
Mass	895 g

weight, range, power. Take E-Hang 184 for example, the power density of battery pack is  $157 \text{ Wh kg}^{-1}$ , while the power density of the battery module in this paper is more than  $240 \text{ Wh kg}^{-1}$ .<sup>137</sup> Considering a 70% efficiency from the module to battery pack, the power density of the pack in this paper is about  $170 \text{ Wh kg}^{-1}$ , which is a little higher than that of E-Hang 184. Therefore, the battery module in this paper is suitable for the simulation analysis under flying car operating conditions. The spacing between each battery cell was 1 mm. Thermal pad was placed between the module and FHP to reduce contact thermal resistance. So in this paper, contact thermal resistance was considered negligible during simulation. Table 2 enlists the major structural parameters of FHP. The shell of FHP was made of aluminum because of its low density and high thermal conductivity. Acetone was selected as the phase change working medium of FHP because of its working temperature and compatibility with aluminum. Air cooling was used for heat dissipation at the condensation section. A series of cooling fins were arranged next to each other on the condensation section to expand the heat transfer area and improve heat dissipation effect. The rectangular cooling fins were made of aluminum (same as the FHP shell). Table 3 presents the structural parameters of cooling fins.

TABLE 2 Key structural parameters of FHP

Parameters	Value	Units
FHP length	0.44	m
Evaporator length	0.331	m
Adiabatic section length	0.012	m
Condenser length	0.097	m
FHP width	0.148	m
Total thickness of FHP	5	mm
Thickness of shell	1	mm
Thickness of wick	1.5	mm
Thickness of vapor channel	1.5	mm

TABLE 3 Structural parameters of cooling fins

Parameters	Value	Units
Number of fin	25	/
Width of fin	0.148	m
Height of fin	0.08	m
Thickness of fin	1	mm
Spacing between fins	3	mm

## 2.2 | FHP-based BTMS simulation model

This study used a CFD model to simulate the thermal behavior of batteries under different working conditions. Each model of the BMTS components is described below, including the battery model, FHP model, and coolant model. The following assumptions are presented to simplify the model's simulation:

- The thermal conductivity of the battery material is heterogeneous in different directions. Moreover, the specific heat capacity and thermal conductivity were constant and temperature independent.

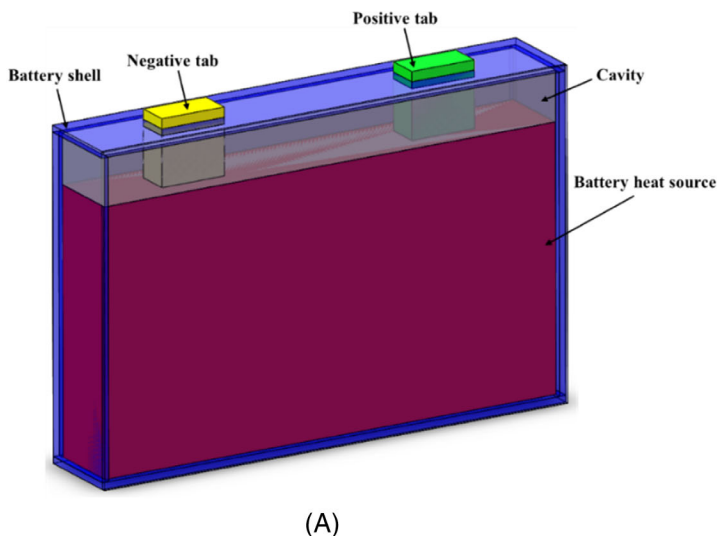
- b. The heat generation was uniformly distributed in the cell.
- c. Heat convection and radiation in the cell were considered negligible. Only the convective heat transfer was considered on battery cell, FHP, and cooling fins surface with the external environment. Moreover, the contact thermal resistance was neglected between batteries and FHP.
- d. The FHP works below its heat transfer limitation. The heat transfer performance of the FHP is unaffected by its setting direction. Phase change on the wick-vapor interface and working medium flow inside FHP were ignored.
- e. The thermal conductivity of the FHP is assumed constant. Its working performance was unaffected by the temperature, battery heat generation, and heat dissipation structures.

### 2.2.1 | Battery thermal model

A single battery cell was divided into the following parts: battery shell, battery heat source, positive tab (aluminum), negative tab (nickel), and cavity. Figure 2 (A) presents the physical model of the single battery cell. In the simulation, the following energy equation was solved to obtain the temperature distribution<sup>38</sup>:

$$\rho C_p \frac{\partial T}{\partial t} = \frac{\partial}{\partial x} \left( \lambda_x \frac{\partial T}{\partial x} \right) + \frac{\partial}{\partial y} \left( \lambda_y \frac{\partial T}{\partial y} \right) + \frac{\partial}{\partial z} \left( \lambda_z \frac{\partial T}{\partial z} \right) + q \quad (1)$$

where  $\rho$ ,  $C_p$  and  $\lambda$  denote the density, specific heat, and thermal conductivity of the battery, respectively.



$T$  denotes the battery temperature and  $q$  represents the heat generation rate in the unit volume of the battery cell.

The heat was generated in the cell by two primary heat sources, presented on the right side of Equation (2). The first term refers to the irreversible joule heat created by the internal resistance of the battery, whereas the second term refers to the reversible heat generated by the entropy change.<sup>39</sup>

$$Q = I(U - U_{OCV}) + IT \frac{dU_{OCV}}{dT} \quad (2)$$

where  $Q$  denotes the total heat generation rate in the battery.  $I$  is the charging or discharging current,  $U$  and  $U_{OCV}$  are respectively the terminal and open-circuit voltage of the battery.  $dU_{OCV}/dT$  represents the battery entropy coefficient. According to the related studies,<sup>40,41</sup> the irreversible joule heat can be expressed as  $I^2(R_o + R_p)$  in this simulation. Then,  $q$  is rewritten as:

$$q = \frac{1}{V} \left[ I^2(R_o + R_p) + IT \frac{dU_{OCV}}{dT} \right] \quad (3)$$

where  $V$  is the cell volume.  $R_o$  and  $R_p$  denote the ohmic resistance and polarization resistance of the battery, respectively. These parameters shared a nonlinear relationship and were affected by state of charge (SOC), temperature and current of the battery. This study established a resistance-based battery model to reflect this relationship. The detailed modelling process and experimental validation were described in previous studies.<sup>42</sup> Figure 2B shows the heat generation rate of the battery cell under natural convection from 90% SOC to 10% SOC at different discharge rates. The heat generation rate

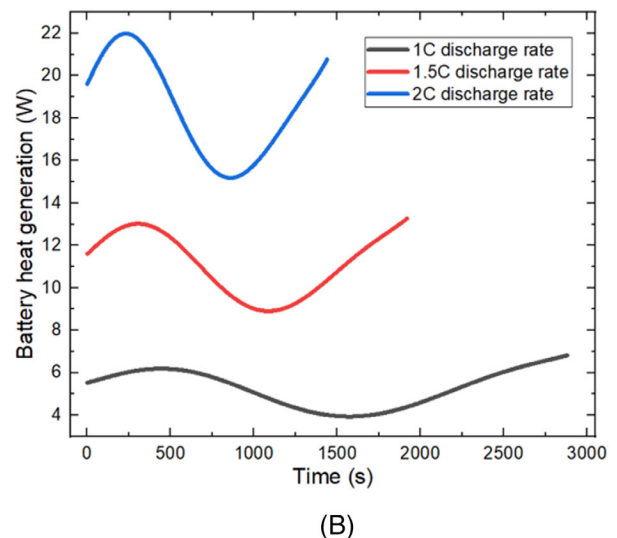


FIGURE 2 (A) Physical model of a battery cell, (B) Heat generation of a battery cell under different discharge rates



of the battery decreases at around 20% DOD (depth of discharge) and begins to increase gradually at around 60% DOD. That's because the internal resistance decreases gradually before the middle stage of the discharge (about 50% DOD), then increases gradually, which leads to the tendency of heat generation rate in Figure 2B.<sup>42</sup>

### 2.2.2 | FHP model

Figure 3 shows the internal structure FHP in this study's simulation, including aluminum shell, sintered wick, and vapor channel. The working principle of FHP is shown as follows. The heat generated by the batteries was transferred to the evaporation section of FHP. The working fluid absorbed the heat by phase change and conducted heat into condensation section because of pressure drop. Finally, the heat was dissipated by the cooling air at the condensation section. Then the working fluid flows back to the evaporation section by the wick capillary force. As previously mentioned, the FHP was considered an isothermal conductor with constant thermal conductivity. Table 4 enlists the thermal properties of the materials used in the BTMS. The battery physical parameters are obtained by experimental tests. The calculating process of FHP parameters, including density, specific heat, and thermal conductivity is based on the following equations:

$$\rho_{\text{FHP}} = \frac{\rho_{\text{Al}}V_{\text{Al}} + \rho_{\text{w}}V_{\text{w}} + \rho_{\text{v}}V_{\text{v}}}{V_{\text{FHP}}} \quad (4)$$

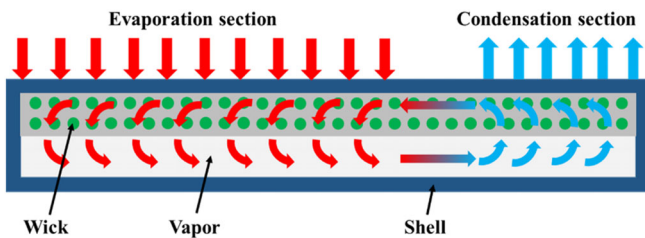


FIGURE 3 Internal structure of the FHP

Material	$\rho$ ( $\text{kg m}^{-3}$ )	$C_p$ ( $\text{J kg}^{-1} \text{K}^{-1}$ )	$\lambda$ ( $\text{W m}^{-1} \text{K}^{-1}$ )
Battery	2519	1022.8	1.0962 (z axis) 22.4459 (x and y axis)
Aluminum	2719	871	202.4
Nickel	8900	460.6	91.74
Air	1.225	1006.43	0.0242
FHP	1655	910	2000

TABLE 4 Properties of the materials

$$C_{p,\text{FHP}} = \frac{C_{p,\text{Al}}m_{\text{Al}} + C_{p,\text{w}}m_{\text{w}} + C_{p,\text{v}}m_{\text{v}}}{m_{\text{FHP}}} \quad (5)$$

$$\lambda_{\text{FHP}} = \frac{l_{\text{FHP}}}{R_{\text{FHP}}S_{\text{FHP}}} \quad (6)$$

where the subscripts FHP, s, w, and v respectively denote the parameters of FHP (total), aluminum shell, wick, and vapor channel.  $l$  and  $S$  are the length and sectional area, respectively.  $R$  is the FHP thermal resistance which is calculated based on the thermal resistance model in our previous study in Ref.<sup>29</sup> For batteries under different discharge rates from 2C to 4C, the thermal conductivity of FHP is around 2000 ( $\pm 20\%$ )  $\text{W}\cdot\text{m}^{-1}\cdot\text{K}^{-1}$ . So in this paper, the thermal conductivity is set 2000  $\text{W}\cdot\text{m}^{-1}\cdot\text{K}^{-1}$ .

### 2.2.3 | Coolant model

Air was supplied to dissipate heat at the condensation section of FHP. A total of 25 cooling fins were inserted on the FHP, and the schematic diagram is presented in Figure 1. In the air-cooled BTMS, the Reynolds number of the inlet flow was usually larger than  $10^4$ ; hence, the status of the airflow was turbulence.<sup>43</sup> Assuming that the cooling air was incompressible, the Navier-Stokes equations with the  $k - \epsilon$  model was adopted to simulate the airflow along the cooling fins in the BTMS:

$$\frac{\partial \rho_a}{\partial t} + \nabla \cdot (\rho_a \vec{v}) = 0 \quad (7)$$

$$\frac{\partial \vec{v}}{\partial t} + (\vec{v} \cdot \nabla) \vec{v} = -\frac{1}{\rho_a} \nabla p + \nu \nabla^2 \vec{v} \quad (8)$$

$$\frac{\partial T_a}{\partial t} + (\vec{v} \cdot \nabla) T_a = \frac{k_a}{\rho_a C_{p,a}} \nabla^2 T_a \quad (9)$$

where  $\rho$ ,  $p$ ,  $T$ ,  $\lambda$ , and  $\nu$  denote the density, pressure, temperature, thermal conductivity and kinematic viscosity,

respectively, and  $\vec{v}$  is the velocity vector. The subscript  $a$  refers to air.  $C_{p,a}$  is the air-specific heat capacity. The control equations of the whole system are discretized by finite-volume method. SIMPLE algorithm is used as the scheme of the solvers. The spatial discretization methods and the boundary conditions are selected and set in ANSYS Fluent GUI (graphical user interface).

## 2.2.4 | Initial and boundary conditions

The initial temperature of the BTMS system was 20°C, which was same as the ambient temperature. The batteries discharge from 90% SOC to 10% SOC. The inlet flow of the cooling air was set as the velocity inlet. The outlet was set to be a pressure outlet whose temperature was equal to the ambient temperature. The contacts between batteries and FHP, cooling fins and FHP, and cooling air and FHP were set as coupled walls. The bottom of FHP was set as adiabatic, whereas the other system surfaces were under the natural convection condition with heat transfer coefficient value of  $5 \text{ W}\cdot\text{m}^{-2}\cdot\text{K}^{-1}$ .

## 2.2.5 | Computational grid

This study conducted grid independence tests to ensure the simulation's accuracy. ANSYS FLUENT with user defined function programmed by the authors was used to solve battery thermal performance with the FHP-based BTMS. A grid independence test was conducted to determine the suitable grid number for the simulation. In the verification cases, the battery discharge rate was 3C and the inlet velocity was  $10 \text{ m s}^{-1}$ . The highest temperature of the module in discharging process was selected as the assessment criteria, and the results are presented in Figure 4. Maximum temperature of batteries changed no more than 0.1°C when the grid number was from  $5.2 \times 10^5$  to  $1.4 \times 10^6$ . Therefore, the grid number  $5.2 \times 10^5$  was chosen, and the grid division method, in this case, was applied to other simulations under different FHP configurations in Section 4.

## 3 | MODEL VALIDATION

The simulation results were compared with the following experimental data to validate the proposed model. Figure 5 shows the schematic diagram of the experimental system. It comprises an FHP with 25 rectangular fins, a battery module consisting of 12 cells, a battery tester, a temperature measurement and acquisition system, and an air-cooling system. The battery cells were placed in parallel on the surface of FHP. The battery tester

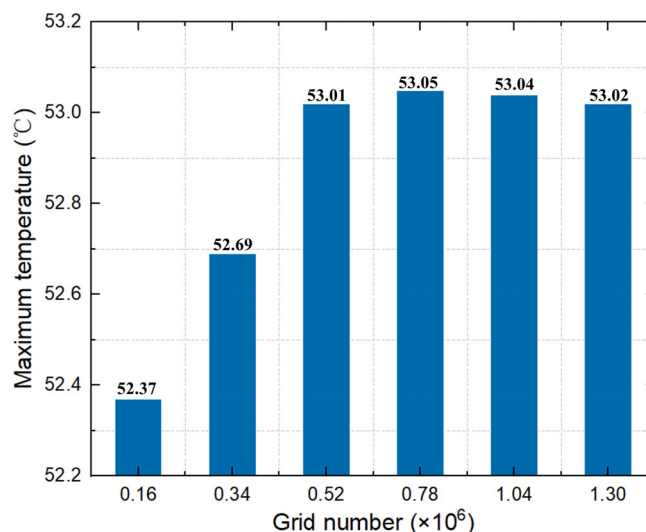


FIGURE 4 Results of the grid independence test

(Digatron EVT300-0600) was used to provide external load to the battery module and collect the current and voltage data during the charging or discharging conditions. The relative uncertainty of the battery tester was  $<0.1\%$  of the measurements. The temperatures of the batteries were measured by K-type thermocouples and the testing error was  $0.15 + 0.002|T|^\circ\text{C}$ . In total, 24 thermocouples were placed at the face centroid on both sides of each single battery cell, which is illustrated in Figure 6. The temperature data were gathered by the data collector (Agilent 34972A) and then transmitted to a computer at an interval of 1 s. The thermal grease with a thermal conductivity more than  $3.0 \text{ W}\cdot\text{m}^{-1}\cdot\text{K}^{-1}$  was covered on FHP evaporation section to reduce the contact thermal resistance between the module and FHP. Cooling air was supplied at condensation section with the assistance of an electric fan and air channel. An anemograph was inserted through the air channel to measure the velocity. The bottom of FHP was covered with thermal insulation material to prevent heat transfer to the ground. The cooling air velocity was  $5 \text{ m s}^{-1}$  and the ambient temperature was the same as the BMTS's initial temperature (20°C). The battery module was placed in the laboratory with an ambient temperature of about 20°C, and the boundary conditions could be approximately equivalent to natural convection condition. As the laboratory was a relatively large space and the indoor temperature was maintained by air-conditioning, it could be approximated that the ambient temperature was 20°C. After each discharging and charging process, the battery module was let stand in the environment for more than 10 hours. When the batteries were cooled down and the temperature measurement data of thermocouples was stable within the range of  $20 \pm 0.5^\circ\text{C}$ , the next experimental discharging process could be started. We used Schultz and Cole<sup>44</sup> method to

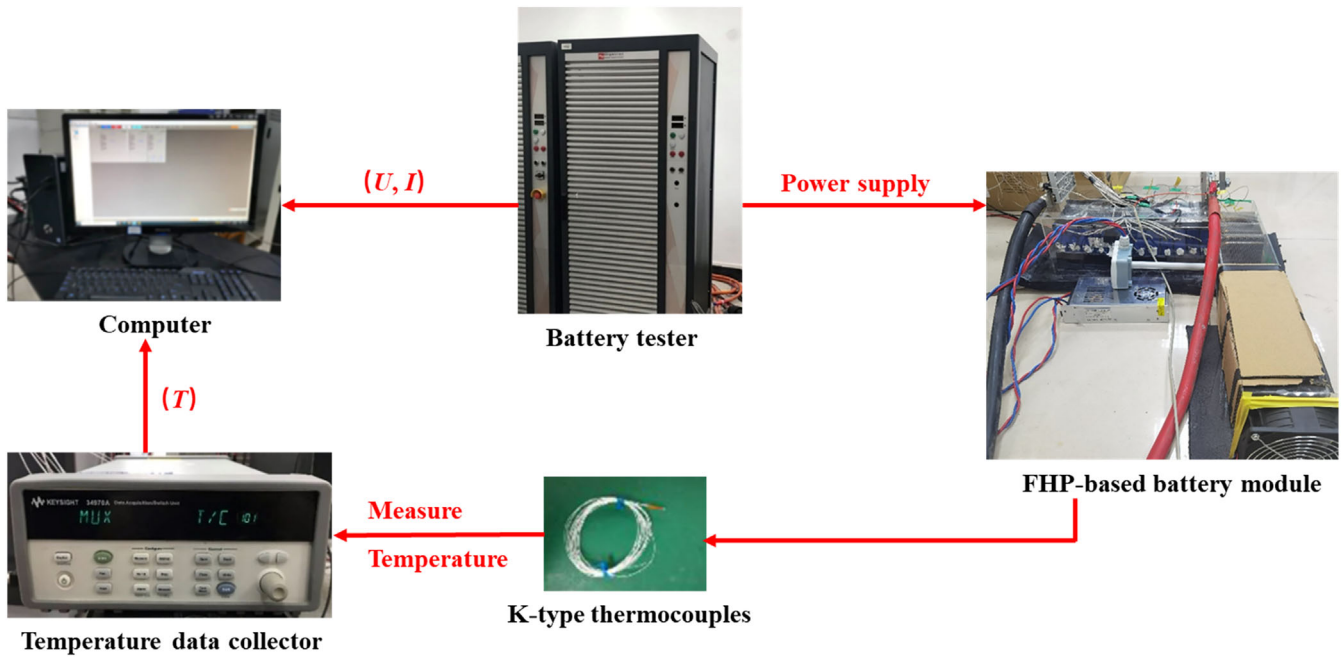


FIGURE 5 Schematic diagram of the experimental system devices

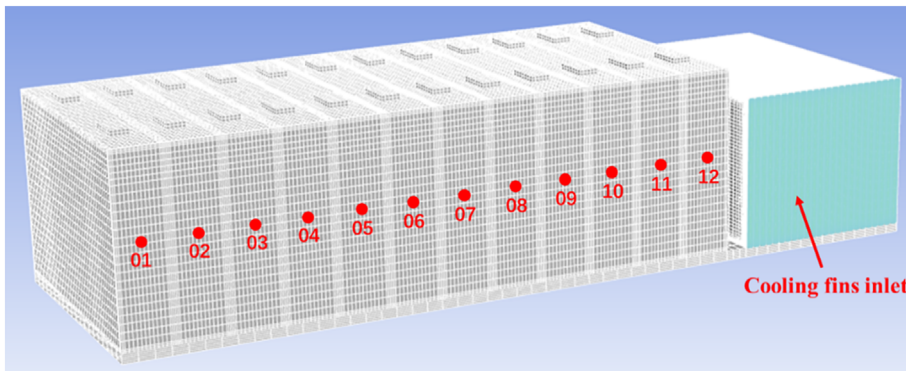


FIGURE 6 Schematic diagram of the temperature measuring points of the batteries

calculate the measurement uncertainty. The maximum relative uncertainty was  $<1.35\%$ .

The battery discharges at a  $1.5C$  rate from  $90\%$  SOC to  $10\%$  SOC in our experiment. Figure 7 shows the comparison of simulation results and experimental data for the battery temperature distribution at the end of discharging process. Figure 7A shows the surface temperature from measure point 1 to 12 corresponding to battery numbers 1 to 12, respectively. The calculated results and experimental data were close with a deviation of  $3^\circ\text{C}$ . The reason is that as the battery temperature rises in experimental process, the ambient temperature near the battery module rises synchronously, which is around  $23^\circ\text{C}$  at the end of discharge. This may result in a relatively worse heat dissipation effect. Also, we can find that the temperature of the fourth battery cell is relatively lower in Figure 7A. The reason maybe that the data measured by thermal couple has measurement uncertainty as error bar shows in Figure 7A. The temperature measured

in the fourth battery maybe lower than the true value and the deviation maybe relatively large. On the other hand, there may be some operation problems during the experiment, such as poor contact between the fourth thermocouple and the battery cell. We also compared the temperature development and heat dissipation of battery cell 1 between experimental and simulation results. The heat dissipation of battery cell is calculated by Equation [10]:

$$Q_{\text{dis}} = Q - \rho C_p \frac{\partial T}{\partial t} \quad (10)$$

where,  $Q_{\text{dis}}$  denotes the heat dissipation of the battery cell. Figure 7B presents the temperature development of measure point 1 on the surface of battery 1 while Figure 7C shows the comparison of battery 1 heat dissipation between experiment and simulation. The results were relatively similar at the first half of discharging.



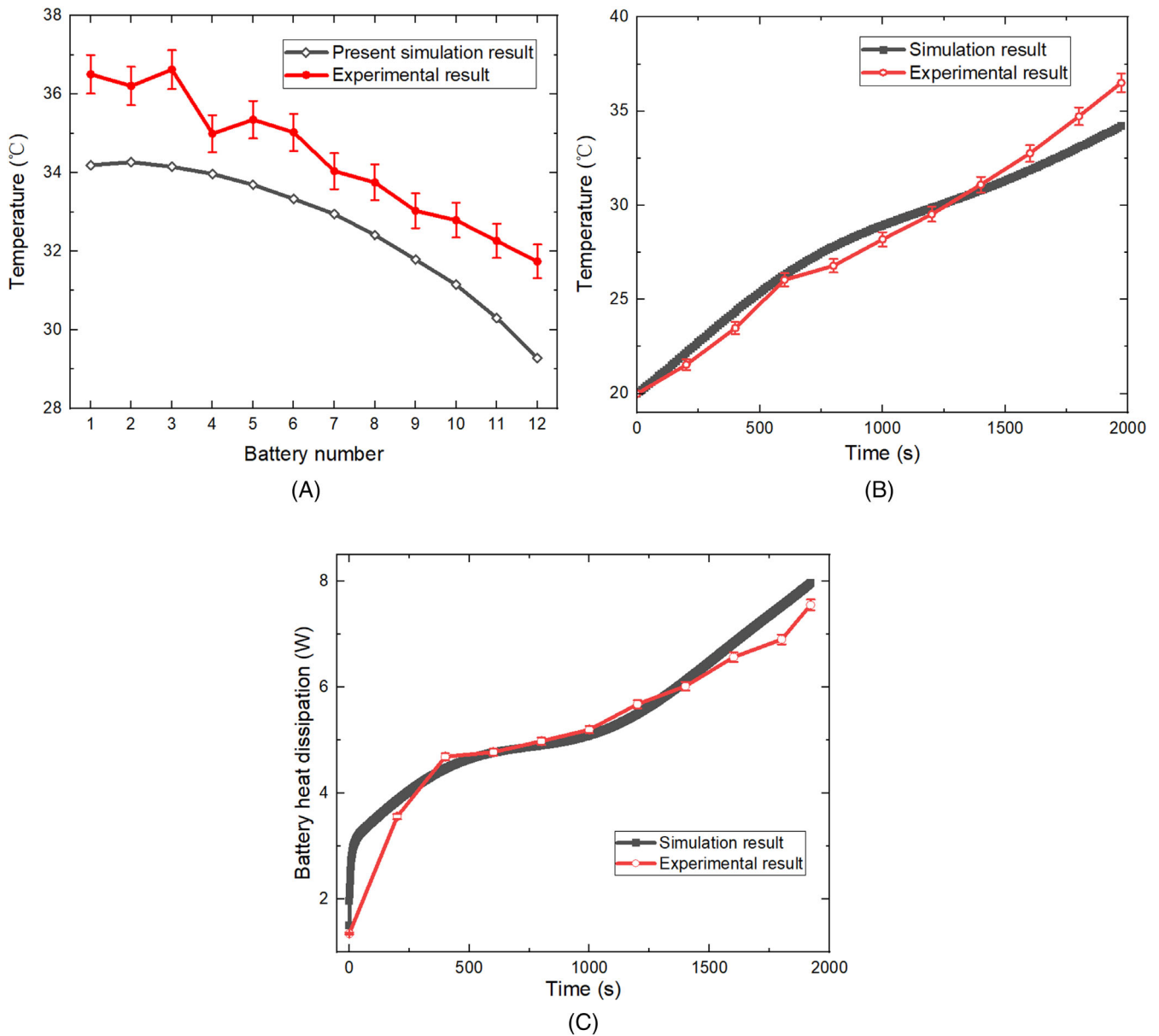


**FIGURE 7** (A) Temperature distribution of 12 battery cells at the end of 1.5C discharge, (B) Temperature development of the measure point 1 in the discharging process, (C) Battery heat dissipation development of battery cell 1 in the discharging process

However, the heat dissipation effect was worse at the end of the experiment, leading to a higher temperature-rising speed than simulation. Based on the above results, the CFD model proposed in this paper can accurately predict the thermal performance of batteries.

## 4 | RESULTS AND DISCUSSION

### 4.1 | Thermal performance of the BTMS at different discharging conditions

The thermal performance of FHP-based BTMS was first analyzed at different battery discharge rates (defined as

rates of the charge or discharge as compared to the nominal capacity of the battery). The initial temperature was set as 20°C, which is same as the ambient temperature. The cooling air with a velocity of 10 m s<sup>-1</sup> was used at the FHP condensation section. The inlet coolant temperature was 20°C. Section 2.2.4 mentioned the other boundary conditions of the simulations. The system's thermal behavior was first simulated under constant discharge rates of 1C, 2C, and 3C. Then, the results were compared to the natural convection condition. Figure 8A presents the maximum temperature development of the FHP system under different discharge rates and boundary conditions. The use of FHP in BTMS can reduce battery maximum temperature effectively. For instance, the

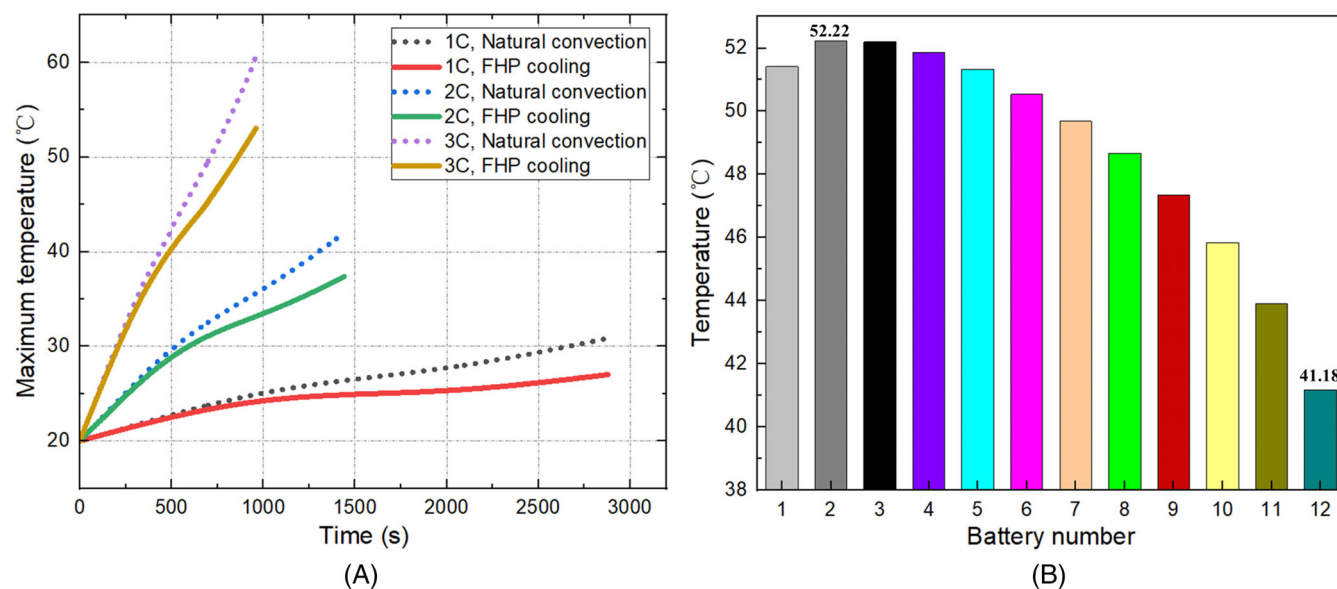


FIGURE 8 (A) Maximum temperature development at different constant discharge rates, (B) Temperature distribution of battery cells in FHP-based BTMS at the end of 3C discharge rate

module's maximum temperature can be controlled under 40°C at 2C discharge rate, which is 4.65°C lower than natural convection. The higher the discharge rate, the greater the decline of the maximum temperature. The maximum temperature drops by 3.85°C under 1C discharge rate and 7.65°C under 3C discharge rate. Figure 8 (B) shows the temperature distribution of each cell at the end of the 3C discharge rate. The battery cell closest to the condensation section has the lowest temperature, whereas the temperature of other battery cells located elsewhere tends to be higher. The reason is that the battery cell next to the cooling fins has the lowest thermal resistance from the evaporation to condensation section, causing temperature to be the lowest. Based on the results shown in Figure 8, the maximum temperature of the system can be seen to exceed 45°C, while the maximum temperature difference was above 5°C under the 3C discharge rate, meaning that the configuration of FHP on this battery module was quite unsuitable. This is because the cooling fins were placed only on the right side of FHP, causing the generated heat of left-side batteries more difficult to dissipate.

Next, the battery thermal performance was considered under transient flying cars working conditions. The flying car battery discharge rate simulated in this paper was referred to the previous related studies.<sup>45,46</sup> The total mass of the flying car is about 3000 kg. The parameters of flying car mission profile are listed in Table 5. Figure 9 presents the discharge rate time curve corresponded to the parameters presented in Table 5. The batteries yield the greatest power in the vertical climb segment, as the

TABLE 5 Parameters of flying car mission profile

Parameters	Value (Property)
Climb acceleration	2 m s <sup>-2</sup>
Maximum climb velocity	4.5 m s <sup>-1</sup>
Flight altitude	500 m
Forward acceleration	2 m s <sup>-2</sup>
Forward velocity	100 km h <sup>-1</sup>
Flight range	50 km

highest discharge rate reaches 4.8C within a short time and keeps more than 4.3C until the end of takeoff segment. The discharge rate of the cell in the forward flight segment turns to be lower, which is maintained at around 1.3C for this period. The discharge rate grows rapidly in the descent segment and settles at around 4.4C. The batteries can provide the transient output power required by the flying car under such a discharge rate, and the whole discharge time is about 30 minutes. In this paper, we started with the battery module instead of the whole battery pack and analyzed the battery thermal characteristics of the module under flying cars' working conditions.

Figure 10 shows maximum temperature rise and temperature difference of the module under flying cars operating conditions. For batteries with natural convection in Figure 10A, the maximum temperature increases rapidly in the beginning and reaches more than 55°C at the end of the climb segment. Then as the discharge rate decreases

to 1.3C, the increasing rate of maximum temperature decreases sharply. The maximum temperature remains almost unchanged in the forward flight segment. When flying car begins landing, the maximum temperature increases with the discharge rate, reaching 61.30°C in the end. After about 200 s in the flying car operation, the maximum temperature of the module consistently exceeds 50°C, which is unfavorable to battery overall performance. For the batteries with FHP-based air cooling, the development rate of maximum temperature in the takeoff and landing segments is not much different from natural convection. The most significant difference between them is

the cruising period. When the battery discharge rate drops to 1.3C in the forward flight segment, the maximum temperature decreases because of heat dissipation in the condensation section. At the end of the forward flight (at 1750 s) segment, the maximum temperature drops to 39.40°C, which is a 46.31% decrease in maximum temperature rise than natural convection. To sum up, the temperature decrease rate ( $^{\circ}\text{C min}^{-1}$ ) of the batteries during the forward flight segment needs to be considered while analyzing the thermal characteristics of the power batteries in the flying car operating condition.

Figure 10B shows the maximum temperature difference of the module under natural convection or FHP cooling. For natural convection, the maximum temperature difference increased at a nearly linear development rate and achieved the highest value of 11.55°C at the end of discharge. For FHP cooling, at the beginning of the high discharge rate, the temperature difference increased rapidly with time because the battery cell near cooling fins had a better heat dissipation effect. Although the discharge rate fell to 1.3C at 200 s, the maximum temperature difference still increased with time delay. The temperature decrease rate of the battery cell further from cooling fins was still lower than that in the area closer to the fins. The maximum temperature difference reached the highest value of 11.43°C at around 600 s. Then, it decreased to around 8°C at the end of discharge. The results showed that the maximum temperature difference appeared during the cruise segment for batteries with FHP cooling. In this simulation case, the maximum temperature difference was greater than the battery temperature uniformity limitation (5°C), which should be improved in the following section.

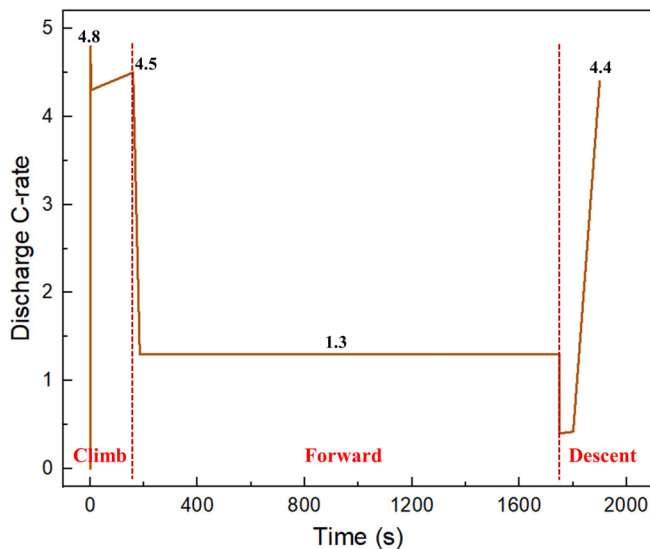


FIGURE 9 Discharge rate curve of power batteries for flying cars

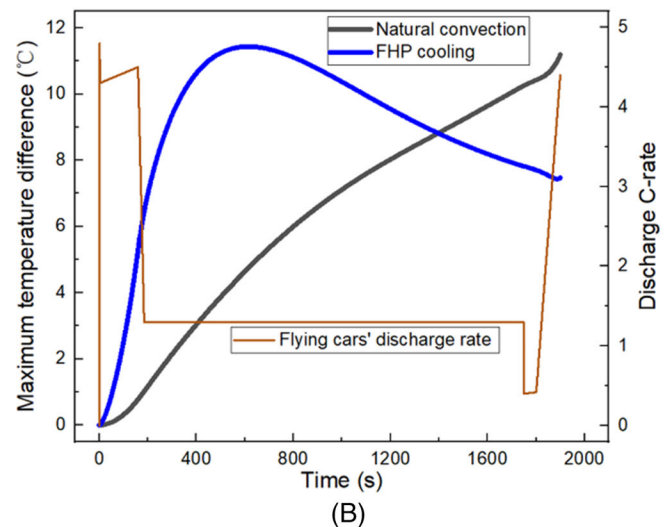
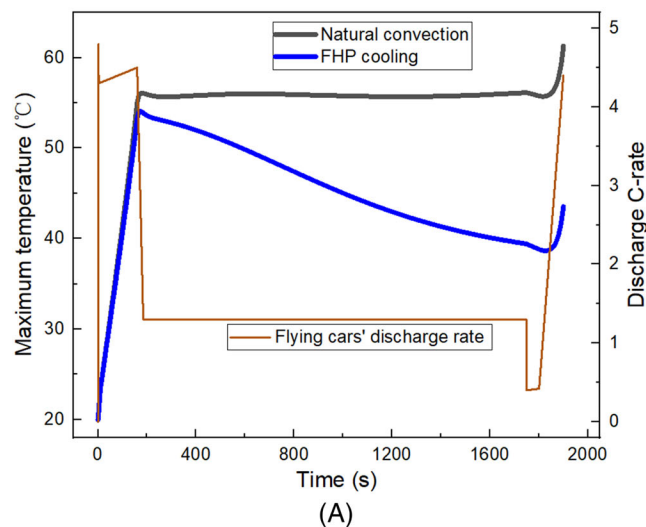


FIGURE 10 The maximum temperature and maximum temperature difference under flying car working conditions: (A) Maximum temperature, (B) Maximum temperature difference

## 4.2 | Influence of different FHP configurations on battery thermal performance

The simulation results for the FHP-based BTMS presented in Section 4.1 revealed that the maximum temperature of the batteries was much higher than 45°C, with the maximum temperature difference being higher than 5°C under both 3C constant discharge rate and flying cars operating conditions. The heat dissipation area of the cooling fins was not large enough, causing a relatively higher temperature under a high discharge rate. On the other hand, the cooling fins at the FHP condensation section were only placed on one side of the battery module, resulting in poor heat dissipation for the battery cells located further away from the cooling fins. Three new FHP-based cooling fins configurations on the battery module (Figure 11) were proposed in this paper to improve the battery thermal performance. For Scheme 2 in Figure 11, the exact specifications of the original cooling fins (Figure 1, Table 3) were placed on both sides of FHP. This will increase the heat dissipation area and shorten the heat diffusion path of the batteries on the module's left side. For Schemes 3 and 4, the cooling fins and the battery module are placed on both sides. It is difficult to directly mount the cooling fins at the surface of the battery for the real BTMS. The fins need to be welded at the condensation section of FHP first, and then dissipate heat of the battery module. This will extend the heat transfer area and strengthen the heat dissipation effect of the system. The heat generated by cells is transferred

from evaporation to condensation section, mainly along the thickness direction of FHP. Table 6 enlists the structural parameters of cooling fins of Schemes 3 and 4. It is worth noting that the weight of the cooling fins is the same for these three systems. Besides, since the thermal conductivity of FHP is a factor that affects the battery thermal characteristics at different FHP configurations, it is set to be the same ( $2000 \text{ W}\cdot\text{m}^{-1}\cdot\text{K}^{-1}$ ) in these simulation cases as a controlled variable.

The battery thermal characteristics were simulated with these new FHP configurations under different working conditions and then compared. Figure 12 shows the thermal performance at the constant 3C discharge rate. Compared to the original FHP configuration, the maximum temperature can be limited to 46.57°C by Scheme 2, which is a 19.6% decrease on the maximum temperature increase. However, the batteries coupled with Schemes 3 and 4 FHP configurations embody a much better thermal performance. The maximum battery temperatures were 42.20°C for Scheme 3 and 41.74°C for

TABLE 6 Structural parameters of cooling fins

Parameters	Scheme 3	Scheme 4
Number of fin	42	84
Width of fin (m)	0.148	0.098
Height of fin (m)	0.0475	0.036
Thickness of fin (mm)	2	2
Spacing between fins (mm)	6	6

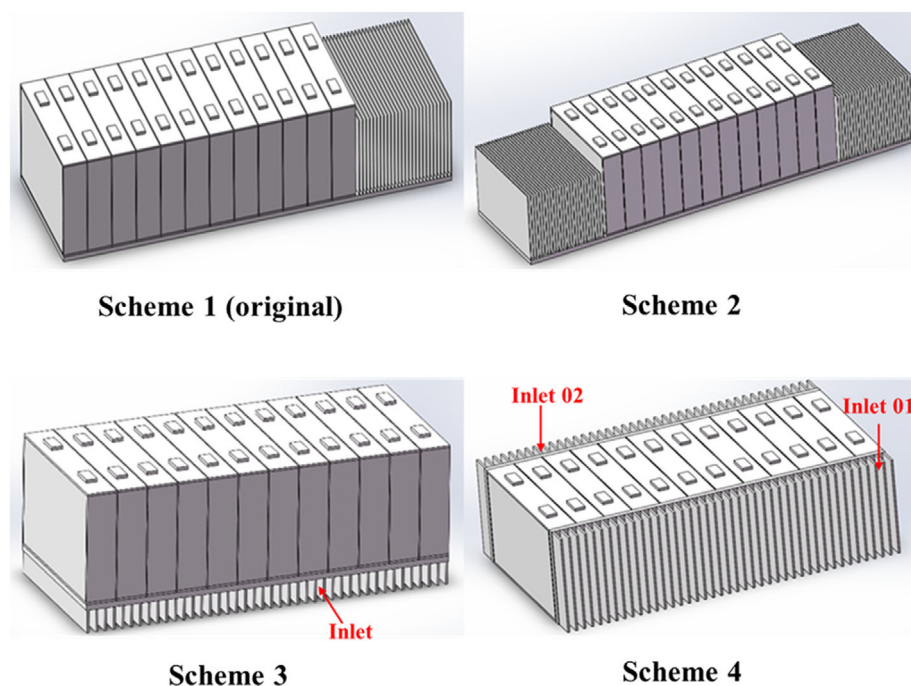
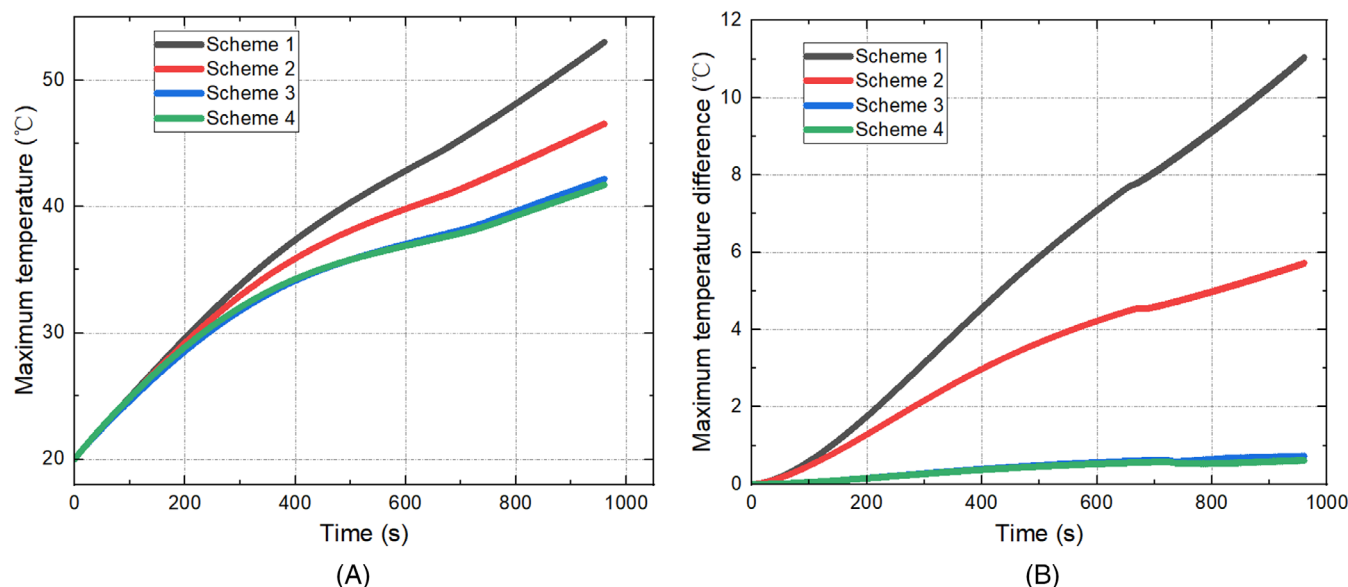


FIGURE 11 Schematic representation of three new FHP-based BTMS configurations



**FIGURE 12** Maximum temperature and maximum temperature difference at the 3C discharge rate under different FHP configurations: (A) Maximum temperature, (B) Maximum temperature difference

batteries coupled with Scheme 4 FHP. As for the maximum temperature difference, Scheme 2 FHP configuration can reduce the value from 11.04°C to 5.71°C. Scheme 3 and 4 FHP configurations can further decrease the maximum temperature differences to 0.72 and 0.63°C, respectively. The Schemes 3 and 4 FHP configurations exhibit a remarkable heat dissipation effect because the maximum temperature rise can be reduced by around 33% and the maximum temperature difference can be decreased by around 94%.

It is obvious that the battery thermal performance is greatly improved for Scheme 3 and Scheme 4. The reason is that the thermal resistance of each battery cell is reduced significantly under Scheme 3 and Scheme 4. For the heat generated in each battery cell, the generated heat is transferred to FHP and then conducted to the condensation section. Then the heat is taken away by the cooling fins. The greater the thermal resistance, the smaller the heat dissipation of the battery cell, and the higher the battery maximum temperature. For Scheme 1, the battery cell on the left side (furthest from the cooling fins) has the largest thermal resistance, as the heat transfer passage is relatively longer than the other battery cells, which causes the higher temperature. For Scheme 2, as a new condensation section is presented, the heat diffusion path for the battery cell on the left side is greatly reduced, which leads to a sharply decrease of the thermal resistance for these battery cells. Then the heat dissipation effect is improved and the maximum temperature is reduced. However, the battery cell in the middle

of the module still has a relatively longer heat passage for heat dissipation, the thermal resistance for the battery cells in the middle is still higher in Scheme 2, which means the maximum temperature reduces slightly in these middle battery cells. For Scheme 3 and Scheme 4, the cooling fins are placed under FHP and the heat generated by the battery cells can be conducted and dissipated directly along the thickness of the FHP. Each battery cell (not only at left side but also in the middle) of the module has a lower thermal resistance for heat transfer, so the maximum temperature of the module can be further reduced compared to Scheme 2. As for the maximum temperature difference, the thermal resistance for each battery cell are uniformly distributed. Then the heat dissipation rate for each battery cell is approximately equal to each other, which leads to a lower temperature difference for Scheme 3 and Scheme 4.

The thermal behavior of BTMS was analyzed under flying car operating conditions, whose results are shown in Figure 13. Similar to the conclusions in Figure 13, the batteries coupled with Schemes 3 and 4 FHP configurations have a lower temperature rise and a better temperature uniformity. For the maximum temperature curve in Figure 13 (A), although the maximum temperature at the end of climb segment exceeds 50°C for all the FHP configurations, the batteries by Schemes 3 and 4 have a higher temperature drop rate during the forward flight segment. The maximum temperature dropped below 45°C in <3 minutes while cruising and was finally kept below 30°C at the end of the flight forward segment.



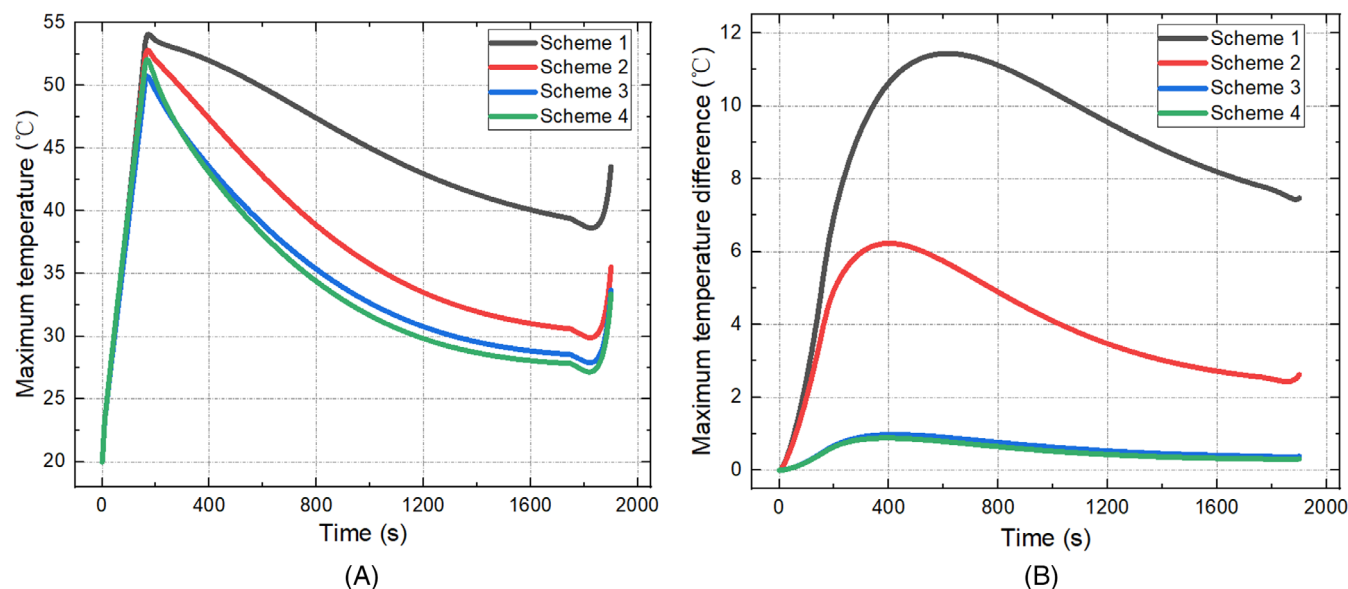


FIGURE 13 Maximum temperature and maximum temperature difference at the flying car's discharge rate under different FHP schemes: (A) Maximum temperature, (B) Maximum temperature difference

Although the discharge rate rises during the descent segment at the end of discharge, the maximum temperature still does not exceed 45°C. Moreover, maximum temperature difference shown in Figure 13B can also be limited to under 1°C by using Schemes 3 and 4 FHP configurations. The reason of different FHP heat dissipation performance under different schemes are similar to the analysis in the last paragraph.

To summarize, Schemes 3 and 4 FHP configurations can improve the battery overall thermal performance at both 3C constant discharge rate and transient flying cars operating conditions. The reason for this is that the cooling fins and battery module in these two configurations were installed on the opposite surfaces of FHP. The heat generated by each cell can be dissipated efficiently along thickness direction, greatly enhancing the heat dissipation effect of battery cells, especially those in the middle of the module. This will further lower the maximum temperature of the module. Furthermore, cooling fins were arranged evenly on the FHP's condensation section. The symmetrical BTMS structure can also greatly reduce the maximum temperature difference among the cells. In contrast, the heat dissipation effect of Scheme 4 was slightly better than that of Scheme 3. Given that the FHP of Scheme 3 was arranged at the bottom of the battery and the FHP of Scheme 4 was arranged on both sides of the battery, the FHP of Scheme 3 has a much simpler layout structure. Therefore, Scheme 3 was used as the FHP-based BTMS configuration for the battery pack. The parametric analysis was conducted further in Section 4.3.

### 4.3 | Heat dissipation effect of FHP-based air cooling on the battery pack

#### 4.3.1 | Battery thermal performance under different discharge rates

As mentioned above, Scheme 3 FHP-based cooling fins were chosen for BTMS in a battery pack. Figure 14 shows the schematic representation of this system. Four battery modules (4 parallel and 1 series) were arranged in line with a 10-mm space between them. The battery cells were numbered from 01 to 48 orderly. The FHP (623.2 mm × 331.4 mm × 5 mm) was placed under the bottom of the pack. The cooling fins were mounted under the bottom of FHP, meaning that the battery pack and cooling fins were located at the top and bottom of FHP. The number of cooling fins was 49, whereas the width and height of cooling fins were 331.4 mm and 50 mm, respectively. The other parameters of cooling fins were the same as Scheme 3 presented in Table 6.

The battery thermal performance was first verified under different discharge rates. The results are presented in Figure 15. For the 1C and 2C constant discharge rates, the maximum temperature of the battery pack can be controlled by 25.00 and 33.67°C, respectively. As for 3C discharge rate, the highest temperature was 45.19°C, which was slightly higher than the maximum temperature limitation. For flying cars' transient discharge rate, the maximum temperature was 50.37°C at the end of takeoff segment. Then, the temperature dropped with an average speed of 1.5°C min<sup>-1</sup> at the beginning of the

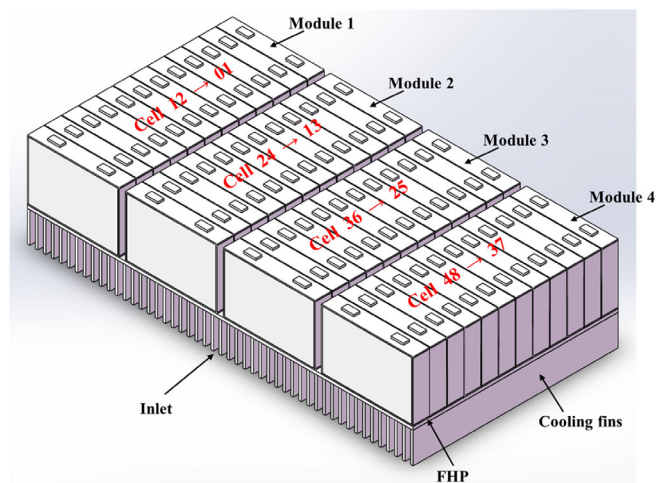


FIGURE 14 Schematic diagram of FHP-based BTMS for the battery pack

forward flight segment. It was finally controlled under 45°C at around 390 s. The abovementioned results demonstrate that the FHP in this configuration can fully meet the thermal characteristics requirements of 1C and 2C discharge rates when applied to BTMS for the battery pack. It can also meet the requirements more than 80% of the time at 3C and different flying car discharge rates.

Figure 16 depicts the temperature distribution of the pack at 3C and flying cars' discharge rate. It can be noticed that the average temperature of the cells located in the center of the battery pack was generally higher than that located on the outside. This is because the nearby batteries affect the convective heat transfer effect between the central cells and the environment. Furthermore, the average temperature of the battery cells tends to increase along the direction in which the cooling airflows. The reason for this result is that the temperature of

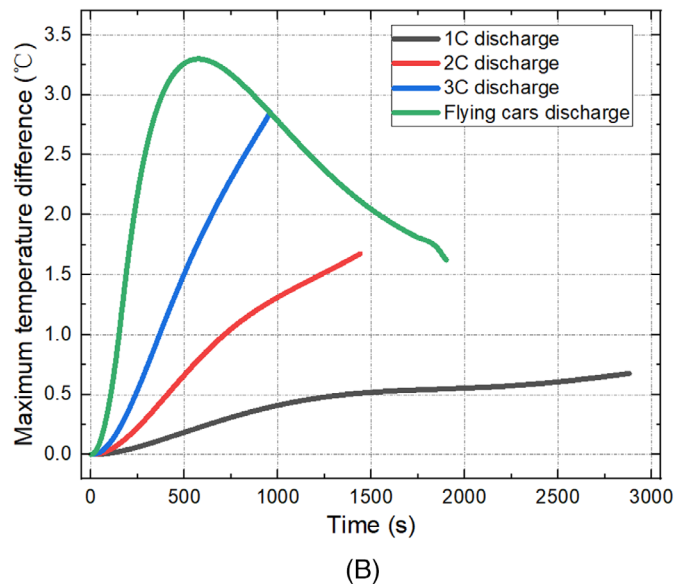
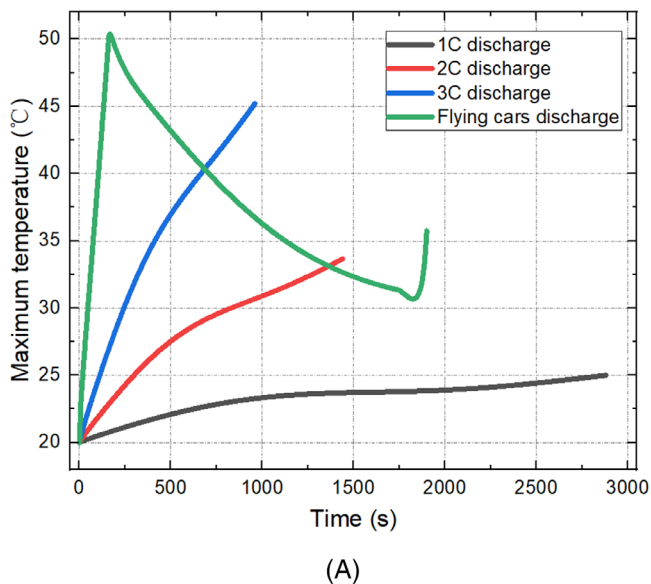


FIGURE 15 Maximum temperature and maximum temperature difference for battery pack under different discharge rates: (A) Maximum temperature, (B) Maximum temperature difference

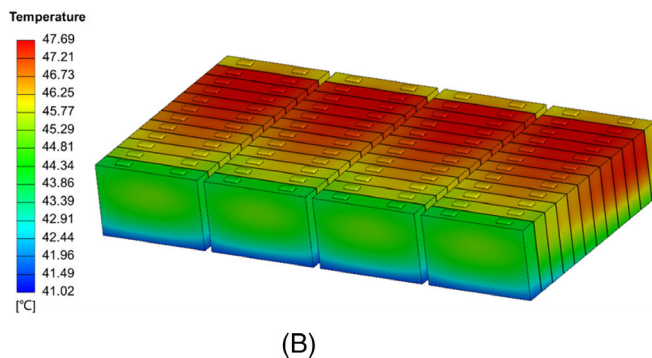
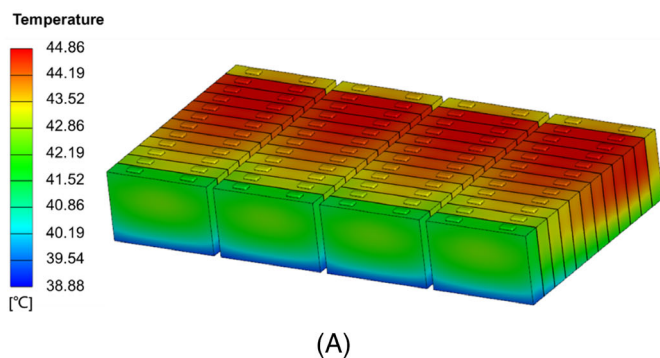


FIGURE 16 Temperature distribution of the battery pack at different discharge rates: (A) At the end of 3C discharge rate, (B) At the end of the climbing segment of flying cars' discharge rate

the cooling air increases continuously along the direction of flow channel, worsening the heat dissipation effect of the cells located further away from the inlet. Therefore, the temperature of the battery cells numbered 14 to 16 and 27 to 29 were higher, and the battery cells numbered 12, 24, 36, and 48 were lower. Also noted that the temperature distribution in each battery module is asymmetric. The battery cells near the inlet have relatively lower temperature while the cells near the outlet higher. That is because the temperature of cooling air increases along the air path from inlet to outlet. The battery cells near the cooling inlet have a relatively better heat dissipation effect, and the average temperature of these battery cells are lower than the others. As the increasing cooling air temperature worsens the heat dissipation effect for the batteries near the outlet, the temperature of the battery cell rises gradually along the air path from inlet to outlet. For the battery cells at the back of the pack (numbered 01, 13, 25, 37), the average temperature decreases because of the convective heat transfer with the environment.

#### 4.3.2 | Battery thermal performance under different inlet velocities

The simulation process of this paper studied the effects of the inlet flow velocity on battery thermal characteristics to improve heat dissipation effect of the FHP system combined cooling fins. The constant 3C discharge rate and transient flying cars discharge rate were adopted for this simulation. Cooling air velocities ranged from 5 to 30 m s<sup>-1</sup>, with an interval of 5 m s<sup>-1</sup>. Figure 17 depicts the maximum temperature and maximum temperature

difference of battery pack at different flow velocities. With the increase in the flow velocity, the maximum temperature decreases and the maximum temperature difference increases. However, the variation magnitude of the maximum temperature and maximum temperature difference decreases gradually with the increase in the inlet velocity, meaning that the heat dissipation effect of the system was no longer evident when the airflow velocity increased to a certain level.

Furthermore, for the batteries under flying car discharge conditions, increasing the flow velocity slightly affects the improvement of the maximum temperature. When the velocity increased from 5 to 30 m s<sup>-1</sup>, the highest temperature of the pack only decreased by 0.28°C. This is because the extreme point of maximum temperature arrives at the end of the climbing segment of the flying cars with a value of around 170 s. Because the batteries generate a large amount of heat in a short period of time, the effects of increasing inlet velocity to lower the battery maximum temperature are not noticeable. Therefore, the effects of inlet velocity on temperature decrease rate were further analyzed. The dotted line in Figure 17A represents the decrease rate of the maximum temperature within 1 minute after reaching the extreme point. The greater the inlet velocity is, the faster the temperature drop rate is. However, the impact of inlet velocity on the temperature decrease rate was relatively more apparent. When the flow velocity was increased from 5 to 30 m s<sup>-1</sup>, the maximum temperature decrease rate increased from 1.96 to 2.29°C min<sup>-1</sup>. This outcome indicates that increasing inlet flow velocity can rapidly control the battery temperature below the maximum limitation (45°C).

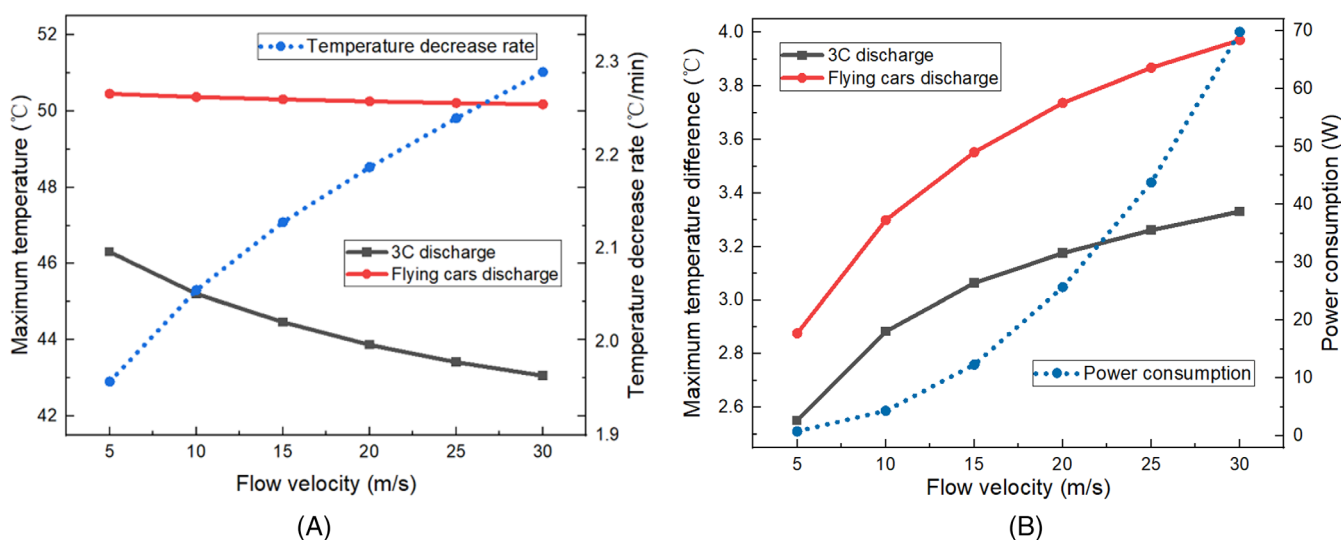


FIGURE 17 Influence of airflow velocity on battery thermal performance at 3C and flying cars' discharge rates: (A) Maximum temperature, (B) Maximum temperature difference

The fan power consumption of the BTMS is an important factor that impacts the specific energy of the battery pack when considering the influence of airflow velocity on battery thermal performance. The ideal fan power consumption can be calculated by the following Equation<sup>18</sup>:

$$P = \dot{V} \Delta P = \dot{V} (P_{\text{in}} - P_{\text{out}}) \quad (11)$$

where  $P$  denotes power,  $\Delta P$  is the pressure drop, and  $\dot{V}$  denotes the inlet volumetric flow rate. The relationship between flow velocity and fan power consumption is presented in Figure 17(B). As the flow velocity increases, the fan power consumption increases and the increasing rate grows faster. When the flow velocity exceeds  $20 \text{ m s}^{-1}$ , the power consumption is  $>25 \text{ W}$ , which may influence the specific energy of the battery pack. Hence, the inlet airflow velocity should be selected considering both battery thermal performance and the fan power consumption.

#### 4.3.3 | Battery thermal performance under different inlet temperatures

This section investigates the thermal characteristics of the pack under different inlet flow temperatures. The cooling air at  $-10, 0, 10, 20,$  and  $30^\circ\text{C}$  were applied to the inlet of the cooling fins at the FHP condensation section. The initial battery pack temperature was kept  $20^\circ\text{C}$  in these simulations. For the inlet temperature with the

value of  $-10^\circ\text{C}, 0^\circ\text{C},$  and  $10^\circ\text{C}$ , considering that flying cars may fly at high altitudes, where the ambient temperature may drop when the flying cars are cruising in the sky. On the other hand, for autumn or winter conditions, the ambient temperature is lower, the batteries are first preheated to the initial temperature ( $20^\circ\text{C}$ ) before the flying car takes off, and then the battery pack is cooled by the ambient airflow. Figure 18 demonstrates the change of battery maximum temperature and maximum temperature difference with the temperature of inlet flow at 3C and flying cars' discharge rate. With the decrease of flow temperature, the battery maximum temperature declines and the maximum temperature difference increases in a nearly linear relationship. Similar to Section 4.2.2, the influence of flow temperature on the temperature decrease rate within 1 minute was further analyzed after reaching the extreme temperature point. The dotted line shows the result in Figure 18A. The maximum temperature decrease rate increased from  $1.86$  to  $2.83^\circ\text{C min}^{-1}$  when the flow temperature decreased from  $30^\circ\text{C}$  to  $-10^\circ\text{C}$ . It should be worth noting that although decreasing the inlet flow temperature can significantly reduce the battery maximum temperature, it will increase the battery maximum temperature difference. For batteries under flying cars' discharging conditions, the maximum temperature difference of the battery exceeds  $5^\circ\text{C}$  when the inlet temperature is  $<0^\circ\text{C}$ . The conclusions of this section can provide a preliminary guidance for the selection of the inlet temperature in certain ways. The flow temperature value should be reasonably selected to meet a better heat transfer effect on the battery thermal performance.

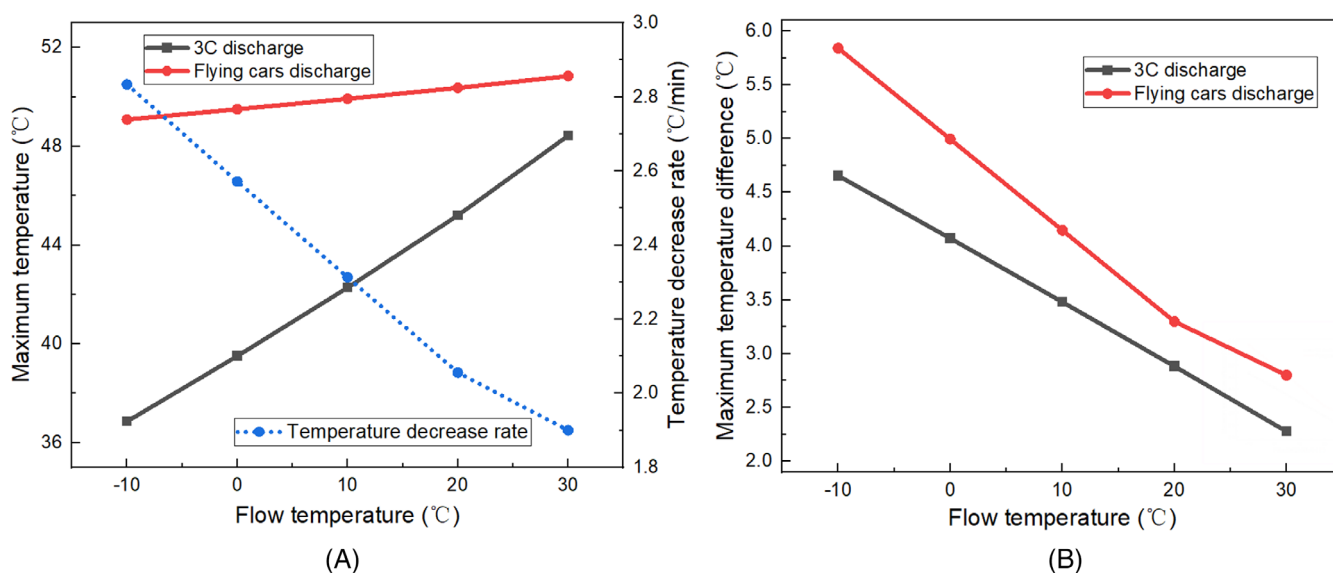


FIGURE 18 Influence of airflow temperature on battery thermal performance at 3C and flying cars' discharge rates: (A) Maximum temperature, (B) Maximum temperature difference



## 5 | CONCLUSIONS AND FUTURE WORK

In summary, a thermal model was established for a battery module cooled by FHP-based airflow. Furthermore, the battery thermal performance was analyzed at different discharging conditions, including the steady constant discharge rate and flying cars' working conditions. Then, different FHP-based cooling fins configurations were proposed and compared among different BTMS schemes. Next, one of the schemes wherein the battery module and cooling fins were relatively arranged at the top and the bottom of FHP was chosen for the battery pack. Finally, the different discharge rate, flow velocity, and flow temperature on the battery thermal performance of the pack were further investigated. Based on the abovementioned analysis, the main conclusions were drawn and listed below:

1. The use of FHP can effectively lower the battery maximum temperature. For flying cars' discharge rate, the maximum temperature appears at the end of the take-off segment, whereas the maximum temperature difference appears during the forward flight segment. Furthermore, the temperature decrease rate of the batteries during the cruising segment needs to be considered while analyzing the battery thermal performance in the flying cars operating conditions.
2. Different configurations of FHP-based air cooling on BTMS can affect maximum temperature and maximum temperature difference of the batteries. The system that places the batteries and cooling fins on the opposite surfaces of FHP can significantly strengthen the heat dissipation effect and then lower the maximum temperature. In contrast, the BTMS with a symmetrical structure can effectively lower the maximum temperature difference among the battery cells.
3. The FHP configuration applied on the battery pack can completely meet the thermal characteristics requirements of 1C and 2C discharge rates. It can also meet the requirements more than 80% of the time at 3C and flying cars' discharge rates.
4. Increasing the inlet flow velocity or decreasing the flow temperature can reduce the maximum temperature while increasing the maximum temperature difference. The flow velocity has a little effect on the maximum temperature for batteries at flying cars' discharge rate, but it can affect the temperature decrease rate. Besides, there was a linear relationship between flow temperature and battery thermal performance.

This paper only verified the possibility of using FHP on BTMS under high battery discharge rate, and

preliminarily discussed the effects of different FHP configurations on the battery thermal performance. Therefore, we only consider the arrangement of cooling fins, and the matching design among the air duct, FHP and battery pack has not been carried out for the whole system right now. After the selection of a better FHP-cooling fins scheme presented in this paper, the detailed design of the BTMS will be performed including air duct design, the selection of fins' structural parameters, the matching design of the whole system. These contents will be reflected in our future works. Moreover, considering that the BTMS system presented in this paper has some difficulties in controlling the battery temperature under 45°C in some simulation cases under high discharge rate. The heat dissipation effect of the system can be further strengthened by optimizing FHP structural parameters of the (such as FHP thickness and length) or the parameters of the cooling fins (such as the thickness and spacing of the fins), and this is also our next step of future work.

### ACKNOWLEDGMENTS

This work was financially supported by the National Natural Science Foundation of China (No. U1864212 and No. U20A20310) and State Key Laboratory of Automotive Safety and Energy (No. ZZ2019-051).

### DATA AVAILABILITY STATEMENT

The data that support the findings of this study are available from the corresponding author upon reasonable request.

### NOMENCLATURE

#### Variables

$C_p$	specific heat [J kg <sup>-1</sup> K <sup>-1</sup> ]
$I$	current [A]
$p$	pressure [Pa]
$q$	heat generation rate per unit volume [W m <sup>-3</sup> ]
$Q$	heat rate [W]
$R$	Resistance [Ω]
$t$	time [s]
$T$	temperature [°C]
$U$	voltage [V]
$V$	Volume [m <sup>3</sup> ]

#### Subscripts

a	air
o	ohmic
p	polarization
x	in x direction
y	in y direction
z	in z direction



**Greek symbols**

- $\lambda$  thermal conductivity [ $\text{W m}^{-1} \text{K}^{-1}$ ]  
 $\mu$  kinematic viscosity [ $\text{m}^2 \text{s}^{-1}$ ]  
 $\rho$  density [ $\text{kg m}^{-3}$ ]

**ORCID**

- Yangjun Zhang  <https://orcid.org/0000-0002-1190-3999>  
 Satyam Panchal  <https://orcid.org/0000-0001-8152-0451>  
 Michael Fowler  <https://orcid.org/0000-0002-9761-0336>  
 Manh-Kien Tran  <https://orcid.org/0000-0001-9937-1749>  
 Yi Xie  <https://orcid.org/0000-0002-1811-2997>

**REFERENCES**

- Zhang Y, Qian Y, Zhuge W, et al. Progress and key technologies of flying cars. *J Autom Safety Energy*. 2020;11(1):1-16.
- Liu M, Qian Y, Luo Y, et al. Lifecycle greenhouse gas emissions and energy cost analysis of flying cars with three different propulsion systems. *J Clean Prod*. 2022;331:129985.
- Warren M, Garbo A, HERNICZEK MTK, et al. Effects of range requirements and battery technology on electric VTOL sizing and operational performance. AIAA Scitech 2019 Forum 2019: 0690.
- Harrison J, Charles D, Zenker J, et al. Using multi-physics system simulation to predict battery pack thermal performance and risk of thermal runaway during eVTOL aircraft operations. In: Proceedings of the 2019 AIAA/IEEE electric aircraft technologies symposium (EATS), F 22–24 Aug. 2019; 2019.
- Panchal S, Dincer I, Agelin-Chaab M, Fraser R, Fowler M. Design and simulation of a lithium-ion battery at large C-rates and varying boundary conditions through heat flux distributions. *Measurement*. 2018;116(2):382-390.
- Chen S, Zhang G, Wu C, et al. Multi-objective optimization design for a double-direction liquid heating system-based cell-to-chassis battery module. *Int J Heat Mass Transfer*. 2022;183: 122184.
- Dai H, Zhu L, Zhu J, Wei X, Sun Z. Adaptive Kalman filtering based internal temperature estimation with an equivalent electrical network thermal model for hard-cased batteries. *J Power Sources*. 2015;293:351-365.
- Wu W, Wu W, Qiu X, Wang S. Low-temperature reversible capacity loss and aging mechanism in lithium-ion batteries for different discharge profiles. *Int J Energy Res*. 2018;43(1):243-253.
- Wang C, Zhang G, Li X, et al. Experimental examination of large capacity LiFePO<sub>4</sub> battery pack at high temperature and rapid discharge using novel liquid cooling strategy. *Int J Energy Res*. 2018;42(3):1172-1182.
- Dai H, Jiang B, Hu X, Lin X, Wei X, Pecht M. Advanced battery management strategies for a sustainable energy future: multi-layer design concepts and research trends. *Renew Sustain Energy Rev*. 2021;138:110480.
- Du X, Qian Z, Chen Z, Rao Z. Experimental investigation on mini-channel cooling-based thermal management for Li-ion battery module under different cooling schemes. *Int J Energy Res*. 2018;42(8):2781-2788.
- Zhao Y, Li Q, Zou B, et al. Performance of a liquid cooling-based battery thermal management system with a composite phase change material. *Int J Energy Res*. 2020;44(6):4727-4742.
- Tran T-H, Harmand S, Sahut B. Experimental investigation on heat pipe cooling for hybrid electric vehicle and electric vehicle lithium-ion battery. *J Power Sources*. 2014;265:262-272.
- Dan D, Yao C, Zhang Y, Zhang H, Zeng Z, Xu X. Dynamic thermal behavior of micro heat pipe array-air cooling battery thermal management system based on thermal network model. *Appl Therm Eng*. 2019;162:114183.
- Al-Zareer M, Dincer I, Rosen MA. A review of novel thermal management systems for batteries. *Int J Energy Res*. 2018; 42(10):3182-3205.
- Chen J, Kang S, E J, et al. Effects of different phase change material thermal management strategies on the cooling performance of the power lithium ion batteries: a review. *J Power Sources*. 2019;442:227228.
- Wang Y, Gao Q, Wang G, Lu P, Zhao M, Bao W. A review on research status and key technologies of battery thermal management and its enhanced safety. *Int J Energy Res*. 2018;42(13): 4008-4033.
- Akbarzadeh M, Kalogiannis T, Jaguemont J, et al. A comparative study between air cooling and liquid cooling thermal management systems for a high-energy lithium-ion battery module. *Appl Therm Eng*. 2021;198:117503.
- Jilte RD, Kumar R, Ahmadi MH, Chen L. Battery thermal management system employing phase change material with cell-to-cell air cooling. *Appl Therm Eng*. 2019;161:114199.
- He F, Li X, Zhang G, Zhong G, He J. Experimental investigation of thermal management system for lithium ion batteries module with coupling effect by heat sheets and phase change materials. *Int J Energy Res*. 2018;42(10):3279-3288.
- Lin C, Xu S, Chang G, Liu J. Experiment and simulation of a LiFePO<sub>4</sub> battery pack with a passive thermal management system using composite phase change material and graphite sheets. *J Power Sources*. 2015;275:742-749.
- Wang J, Gan Y, Liang J, Tan M, Li Y. Sensitivity analysis of factors influencing a heat pipe-based thermal management system for a battery module with cylindrical cells. *Appl Therm Eng*. 2019;151:475-485.
- Deng YW, Feng CL, E JQ, et al. Effects of different coolants and cooling strategies on the cooling performance of the power lithium-ion battery system: a review. *Appl Therm Eng*. 2018; 142:10-29.
- Zhou H, Dai C, Liu Y, Fu X, Du Y. Experimental investigation of battery thermal management and safety with heat pipe and immersion phase change liquid. *J Power Sources*. 2020;473: 228545.
- Xie Y, Li H, Li W, et al. Improving thermal performance of battery at high current rate by using embedded heat pipe system. *J Energy Storage*. 2022;46:103809.
- Wu M, Liu K, Wang Y, Wan C. Heat dissipation design for lithium-ion batteries. *J Power Sources*. 2002;109(1):160-166.
- Behi H, Karimi D, Behi M, et al. A new concept of thermal management system in Li-ion battery using air cooling and heat pipe for electric vehicles. *Appl Therm Eng*. 2020;174: 115280.
- Yuan X, Tang A, Shan C, Liu Z, Li J. Experimental investigation on thermal performance of a battery liquid cooling structure coupled with heat pipe. *J Energy Storage*. 2020;32:101984.
- Wang Y, Dan D, Xie Y, Li W, Guo H, Zhang Y. Study on the influence of flat heat pipe structural parameters in battery thermal management system. *Front Energy Res*. 2022;9:1-18.

30. Zhao R, Gu J, Liu J. An experimental study of heat pipe thermal management system with wet cooling method for lithium ion batteries. *J Power Sources*. 2015;273:1089-1097.
31. Gou J, Liu W. Feasibility study on a novel 3D vapor chamber used for Li-ion battery thermal management system of electric vehicle. *Appl Therm Eng*. 2019;152:362-369.
32. Jouhara H, Serey N, Khordehghah N, Bennett R, Almahmoud S, Lester SP. Investigation, development and experimental analyses of a heat pipe based battery thermal management system. *Int J Thermofluids*. 2020;1-2:100004.
33. Behi H, Behi M, Karimi D, et al. Heat pipe air-cooled thermal management system for lithium-ion batteries: high power applications. *Appl Therm Eng*. 2021;183:116240.
34. Zhang Z, Wei K. Experimental and numerical study of a passive thermal management system using flat heat pipes for lithium-ion batteries. *Appl Therm Eng*. 2020;166:114660.
35. Yao M, Gan Y, Liang J, et al. Performance simulation of a heat pipe and refrigerant-based lithium-ion battery thermal management system coupled with electric vehicle air-conditioning. *Appl Therm Eng*. 2021;191:116878.
36. Xu X, Tang W, Fu J, Li R, Sun X. Plate flat heat pipe and liquid-cooled coupled multistage heat dissipation system of Li-ion battery. *Int J Energy Res*. 2019;43(3):1133-1141.
37. Bacchini A, Cestino E. Electric VTOL configurations comparison. *Aerospace*. 2019;6(3):26.
38. Xie Y, Guo H, Li W, Zhang Y, Chen B, Zhang K. Improving battery thermal behavior and consistency by optimizing structure and working parameter. *Appl Therm Eng*. 2021;196:117281.
39. Xie Y, Zheng J, Li W, et al. An improved electrothermal-coupled model for the temperature estimation of an air-cooled battery pack. *Int J Energy Res*. 2019;44(3):2037-2060.
40. Xie Y, Li W, Yang Y, Feng F. A novel resistance-based thermal model for lithium-ion batteries. *Int J Energy Res*. 2018;42(14):4481-4498.
41. Inui Y, Kobayashi Y, Watanabe Y, Watase Y, Kitamura Y. Simulation of temperature distribution in cylindrical and prismatic lithium ion secondary batteries. *Energ Conver Manage*. 2007;48(7):2103-2109.
42. Li W, Xie Y, Zhang Y, et al. A dynamic electro-thermal coupled model for temperature prediction of a prismatic battery considering multiple variables. *Int J Energy Res*. 2020;45(3):4239-4264.
43. Hong S, Zhang X, Chen K, Wang S. Design of flow configuration for parallel air-cooled battery thermal management system with secondary vent. *Int J Heat Mass Transfer*. 2018;116:1204-1212.
44. Sheikholeslami M, Ganji DD. Heat transfer improvement in a double pipe heat exchanger by means of perforated turbulators. *Energ Conver Manage*. 2016;127:112-123.
45. Fredericks WL, Sripad S, Bower GC, Viswanathan V. Performance metrics required of next-generation batteries to electrify vertical takeoff and landing (VTOL) aircraft. *ACS Energy Lett*. 2018;3(12):2989-2994.
46. Luo Y, Qian Y, Zeng Z, Zhang Y. Simulation and analysis of operating characteristics of power battery for flying car utilization. *eTransportation*. 2021;8(100111):100111.

**How to cite this article:** Wang Y, Dan D, Zhang Y, et al. A novel heat dissipation structure based on flat heat pipe for battery thermal management system. *Int J Energy Res*. 2022;46(11):15961-15980. doi:[10.1002/er.8294](https://doi.org/10.1002/er.8294)